Int. J. Electrochem. Sci., 16 **(2021)** Article Number: 211149, doi: 10.20964/2021.11.49

International Journal of ELECTROCHEMICAL SCIENCE
www.electrochemsci.org

Optimization of Fabrication Parameters for High Performance Nano-powder Iron Oxide Production used as Antireflection Coating for Solar Energy Applications

Marwa Fathy[1,*], *Ahmed I. Omran*[2], *Said S. El Egamy*[2]

[1] Electronic Materials Department Advanced Technology and New Materials Research Institute, City of Scientific Research and Technology Applications (SRTA-City), New Borg El-Arab City, P.O. Box 21934, Alexandria, Egypt
[2] Chemistry Department, Faculty of Science, Cairo University.
[*]E-mail: mrwfathy@gmail.com

Received: 16 August 2021 / *Accepted:* 17 September 2021 / *Published:* 10 October 2021

Different architectures of α-Fe_2O_3 were synthesized by a hydrothermal technique without and with the addition of polyethylene oxide (PEO) with different molecular weights. The structural morphology and thermal behavior of the formed α-Fe_2O_3 nanopowder were characterized and analysed. Antireflective coatings (Nano-ARC) of α-Fe_2O_3 were deposited on the glass surface of the ITO substrate using the dip-coating method. The effect of heat treatment temperature on the ARC film was studied. The results showed that well-defined nanobundle-like and nanorod α-Fe_2O_3 architectures were produced when using PEO with a 100k MW in the hydrolysis process and heat-treating at 300 °C. The optical properties of the ARC films were also studied, and the data showed that the maximum transmittance (94.4%) was recorded for the samples prepared using PEO (100 K MW) and heat treatment at 300 °C. The ARC of α-Fe_2O_3 was deposited on the glass surface of the ITO substrate and utilized in nanocrystalline dye-sensitized solar cells (DSSCs). The performance efficiency of the DSSC improved from 6% to 7.6% at normal incidence radiation.

Keywords: Antireflection; α-Fe_2O_3; Hydrothermal technique; Optical transmittance; DSSCs.

1. INTRODUCTION

Antireflection coatings (ARCs) have been widely used to reduce reflection for various applications, such as flat plate displays [1,2], light-emitting diodes (OLEDs) [3], lasers and all types of lenses [4], OLEDs [5] and solar film cells [6].

Dye-sensitized solar cells (DSSCs) are considered to be a next-generation solar cell candidate due to their low cost and simple and easy operation [7]. To improve the efficiency of DSSCs, an ARC layer is deposited on the glass surface of a DSSC. A key issue in the preparation of antireflection coatings

is the deposition of uniform and large surface layers [8]. Various materials are used as ARC single layers [9], such as SiO, SiNx, MgF_2, Al_2O_3, and Ta_2O_5, in addition to multiline coverings such as MgF_2/ZnS, SiO_2/ZnS, and SiO_2/TiO_2. Various preparation methods can be used, such as spin coating [10], dip coating [11–13], layer-by-layer assembly [14,15], lithography [16,17], and steam blending [18].

Recently, different types of metal-oxide nanostructures have provided promising applications in many different fields [19]. Hematite (α-Fe_2O_3) has attracted much attention because of its safety, low cost, and high stability under ambient conditions. It can be synthesized using a variety of techniques, such as chemical precipitation, sol-gel, hydrothermal, electrodeposition, and microwave techniques that support hydrothermal techniques. Various types of α-Fe_2O_3 morphologies, such as nanoparticles, nanorods, nanotubes, hollow spheres, nanoplates, and complex hierarchical structures, have been successfully prepared in a variety of ways. They have been extensively investigated for use in sensory systems (20], lithium batteries [21], catalysts [22], pigments [23], magnetic devices [24] and antireflection coatings [25].

Little work has been reported on the effect of the incorporation of ethylene oxide (EO) and polyethylene oxide (PEO) on the morphology of α-Fe_2O_3 nanoparticles [26]. In the current work, we studied the effect of the incorporation of PEO at different molecular weights (65k, 100k, and 8M) during the preparation process and heat treatment in the production of α-Fe_2O_3 nanomaterials with different architectures. Improving the preparation parameters for obtaining a high optical transmission α-Fe_2O_3 layer deposited on the glass surface of an ITO substrate and using this layer as an ARC were the goals. Additionally, the performance of the DSSC was compared with the results obtained without the ARC.

2. MATERIALS AND METHODS

2.1. Materials

Iron(III) chloride $FeCl_3$, 98%, anhydrous) was purchased from Acros Organics Company, and hydrochloric acid (HCl, 37%) and ethanol (C_2H_5OH, absolute) were purchased from Fisher Chemical Company. Polyethylene oxide (PEO) with different molecular weights (65k, 100k, and 8M MW) was purchased from Aldrich Company. Tin-indium-oxide (ITO)-coated glass plates (Nippon glass with a sheet resistance of 27 Ω/sq, T= 90%) were used. Anatase TiO_2 nanoparticle photoelectrodes and counter electrodes were fabricated as reported in our previous work [25,27–28]. Ruthenium dye (N719) sensitizer was purchased from Solaronix.

2.2. Method

2.2.1. Preparation of α-Fe_2O_3 nanopowder

Aqueous solutions of $FeCl_3$ and HCl (0.01 M) were mixed with a volume ratio of 1:3 (v/v). The solution was kept in a water bath at 90 °C for 24 hr and then cooled at room temperature. The produced suspension was centrifuged at 6000 rpm for 15 min and then dried in vacuum at 60 °C. The same procedure was repeated with the addition of 0.1 g of PEO with different molecular weights (65k, 100k,

and 8M).

The complete hydrolysis reaction is shown in the steps below:[29]

Precipitation of β-FeOOH: $FeCl_3 + 3\ H_2O \longrightarrow \beta\text{-}FeOOH + 3\ HCl + H_2O$ (1)

Dissolution of β-FeOOH: $\beta\text{-}FeOOH + H_2O + 3H^+ \longrightarrow Fe^{3+} + 3H_2O$ (2)

Precipitation of α-Fe_2O_3: $2Fe^{3+} + 3\ H_2O \longrightarrow \alpha\text{-}Fe_2O_3 + 6H^+$ (3)

β-FeOOH was fully transferred to α-Fe_2O_3 within the temperature range of 235 °C to 275 °C with an exothermic effect [30]. The presence of poly(ethylene oxide) reduces the probability of $Fe(OH)_3$ nanoparticle agglomeration; therefore, uniform α-Fe_2O_3 nanoparticles were obtained after aging and heating to complete the phase transformation [30].

The as-prepared sample (termed S1) was treated at 300 °C for 24 hr (termed sample S2) and at 500 °C (termed sample S3). Samples prepared with PEO with an MW of 65k are called S1a, S2a, and S3a. Samples prepared with PEO with an MW of 100k are denoted S1b, S2b, and S3b, while those prepared with PEO with an MW of 8M are denoted S1c, S2c, and S3c.

2.2.2. Deposition of the α-Fe_2O_3 (nano-ARC) thin layer on the glass surface of the ITO substrate

A thin layer of α-Fe_2O_3 was placed on the glass surface of the ITO substrate by the dip-coating technique. An ethanolic solution of α-Fe_2O_3 (0.01 M) was used as the dipping solution, and the immersion time was 5 min. The glass substrate was then withdrawn and dried in air (this was the as-prepared sample). These samples were further heat-treated at 300 °C and 500 °C for 24 hr[25].

2.2.3. DSSC fabrication

Figure 1 shows the DSSC structure. The doctor blade technique [31] was used to prepare the working (photo) electrode (as shown in detail in Kashyout et al. 2010). A thin layer of TiO_2 was formed on the ITO/glass/nano ARC substrate**.** A 0.5 mM ethanolic solution of N719 was used for the sensitization process. The counter electrode was fabricated by depositing a platinum layer (thickness ~2 μm) on the ITO glass substrate using an RF-sputtering method. Electrolyte drops containing a redox system of 0.5 M LiI/50 mM I_2 dissolved in 3-methoxyproponitrile were added between the photoelectrode and counterelectrode. The two electrodes were then pressed together and sealed so that the cell did not leak.

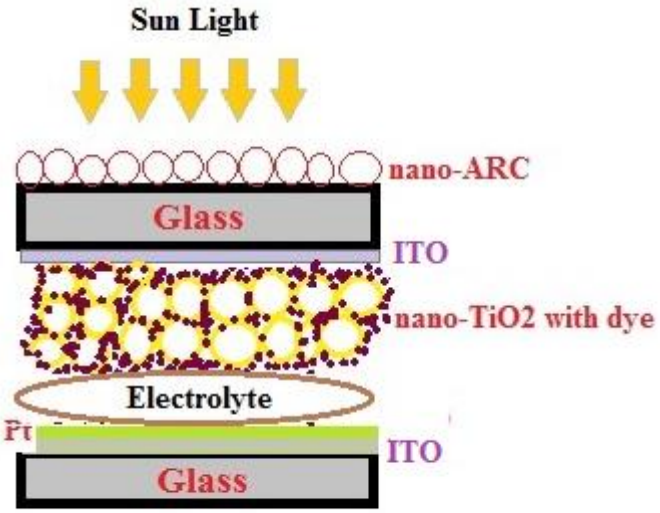

Figure 1. DSSC structure.

2.3. Characterizations

Structural analysis was performed using an X-ray diffractometer (Shimadzu 7000, Japan) and Fourier transform infrared (FT-IR) spectroscopy (Shimadzu FTIR- 8400 S, Japan). Morphological analysis was performed using scanning electron microscopy (JEOL, JSM-6360 LA) and high-resolution transmission electron microscopy (HRTEM) (JEOL JEM-1230, Japan). Optical transmittance was measured (UV–Vis spectrophotometer (LABOMED, INC)). Thermal gravimetric analysis (TGA) was performed using a Shimadzu TGA–50 analyzer (Japan).

The photocurrent density-voltage (J-V) curve of the DSSCs was measured by a solar simulator (PET Photo Emission Tech., Inc. USA). The fill factor (FF) and efficiency of light-to-electricity conversion (η) were calculated by Equations 4 and 5 [31]:

$$FF = ((V_{max}J_{max})/(V_{OC}J_{SC})) \quad (4)$$

$$\eta\% = ((J_{SC}V_{OC}FF/J_o))\, x1\,00 \quad (5)$$

where J_{sc} is the short-circuit current density (mA/cm^2), V_{oc} is the open-circuit voltage (V), and J_{max} (mA/cm^2) and V_{max} (V) are the current density and the voltage in the J-V curve, respectively, at the point of maximum power output. Here, I_o is incident irradiation (W/cm^2).

3. RESULTS AND DISCUSSION

3.1. Characterization of an α-Fe_2O_3 thin film deposited on the glass surface of an ITO substrate

3.1.1. Structural analysis

Figure 2 shows the XRD patterns of the as-prepared thin film samples (S1a, S2a, and S3a). For the as-prepared S1a sample, peaks recorded at 2θ angles were assigned to the lattice planes of the

orthorhombic β-FeOOH phase (according to JCPDS card number 00-018-0639) and other peaks attributed to rhombohedral α-Fe_2O_3 appear according to JCPDS card number 00-033-0664.

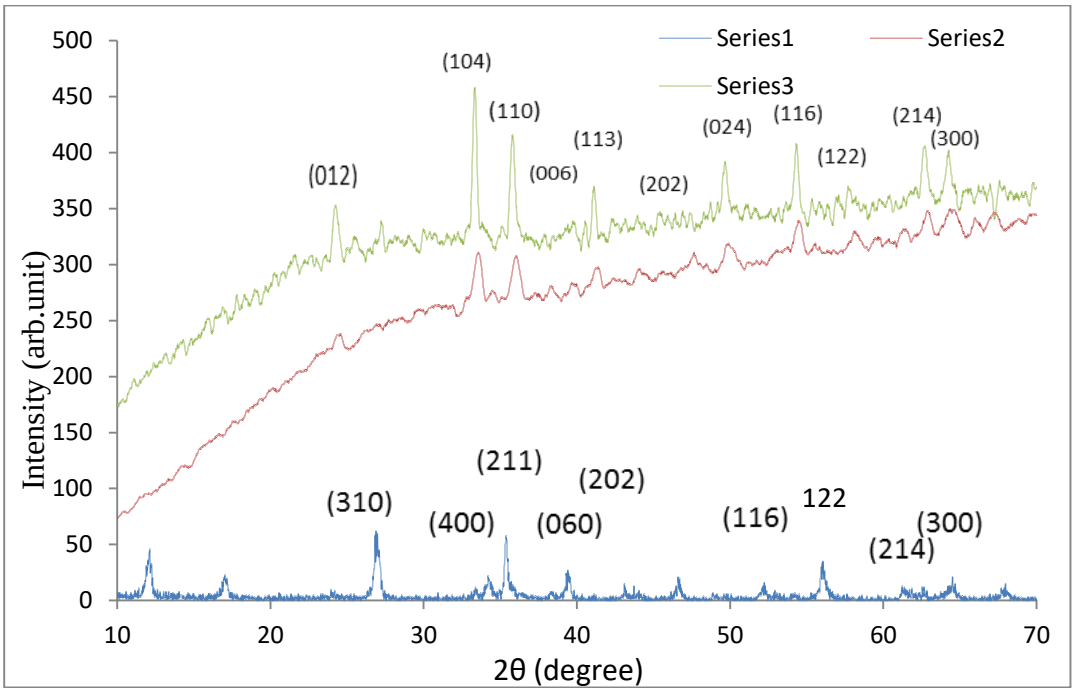

Figure 2. XRD patterns of S1a, S2a, and S3a (where the symbol (a) refers to PEO with an MW of 65k).

For sample S2a (heat treatment at 300 °C for 24 hr), no peaks due to β-FeOOH appeared, indicating the complete transformation of β-FeOOH into rhombohedral α-Fe_2O_3. The S2a sample consisted only of the α-Fe_2O_3 crystalline phase produced according to the overall hydrolysis reactions in Equations (1–3).

For sample S3a (heat treatment at 500ºC for 24 hr.), strong peaks with high intensities (more crystalline) appeared at θ = 24.13°, 33.2°, 35.6°, 40.8°, 49.4°, 57.6°, and 64.13° due to (012), (104), (110), (113), (024), (018) and (300), respectively, which are attributed to the presence of rhombohedral α-Fe_2O_3.

For samples prepared in the presence of PEO with an MW of 65k (S1a), two extra sharp peaks appeared at 2θ = 12.5° and 17.6° according to the crystalline phase of the polymer. Previous work showed two peaks at 2θ = 19.2 and 23.6 [32], while others found only one sharp peak at 2θ = 18.2 when using 10% Fe^{3+} [33] and attributed this to the incorporation of Fe^{3+} ions within the polymeric structure. The position and number of these peaks depend on the PEO:Fe^{3+} ratio. This means that sample S1a consists of β-FeOOH as the main product. The results showed that the S2a sample is less crystalline (more disordered) than the S3a sample. In general, S2a, S2b, and S2c samples are preferable for use as ARCs in solar cell applications.

The crystallite sizes of samples S2a and S3a heat-treated at 300 and 500 °C are 14.3 and 25.5 nm, respectively, as calculated from the Scherrer formula (Equation 6):

$$L = K\lambda/(\beta cos\theta) \quad (6)$$

where L is the size of the crystallite, λ is the wavelength of X-ray radiation (Cu $K_a\alpha$ =0.15418 nm), K is a dimensional shape factor, generally considered to be 0.89, β is the half-maximum height when L is the size of the crystallite, λ is the magnitude of X-ray radiation (Cu Kα = 0.15418 nm), K is the standard deviation factor, generally considered to be 0.89, and β is the half-maximum line width.

Figure 3 shows FTIR spectra of the S1a, S2a, and S3a samples. Figure S1a shows characteristic vibrations of H_2O and Fe-OH bonds. Wide bands at 3340 and 1626 cm^{-1} were attributed to O-H and H-O-H bending vibrations of β-FeOOH and H_2O. Additionally, the 644 and 862 cm^{-1} bands are assigned to the Fe-O vibrational mode of β-FeOOH. Experimental results showed that β-FeOOH formed as an intermediate. The presence of pure PEO was confirmed by the appearance of the absorption band in the 2,950–2,700 cm^{-1} region (unseen) corresponding to the symmetric and asymmetric C-H stretching modes of the CH_2 group. The bandwidth of PEO is reduced by increasing the iron oxide concentration. Vibrational bands can also be seen in the range of 1,240–1,280 cm^{-1}, and the vibrational bands between 850 and 970 cm^{-1} are assigned to CH_2 rocking [34–36].

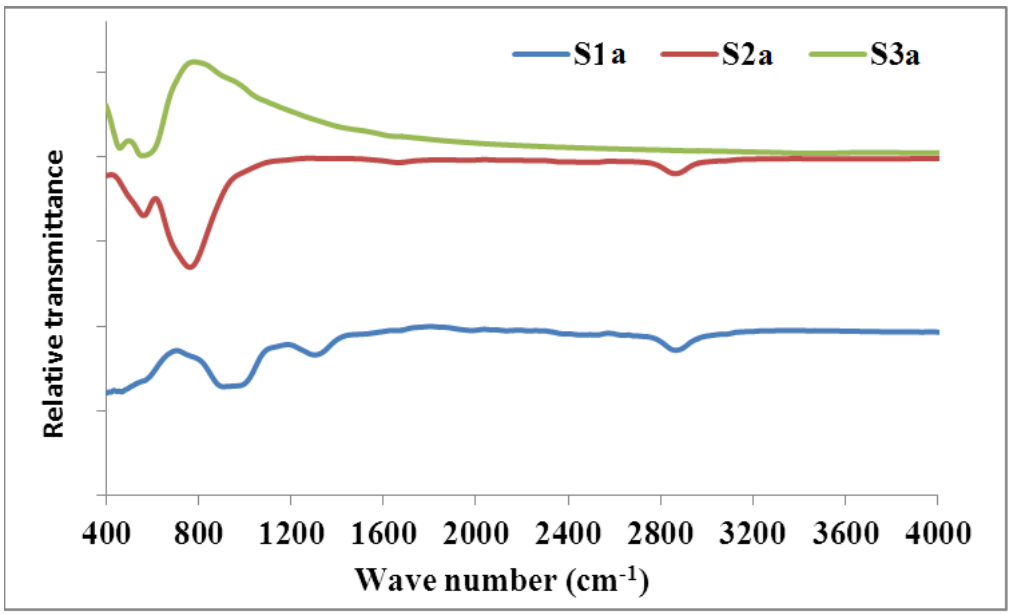

Figure 3. FTIR spectra of S1a, S2a, S3a samples.

For the S2a and S3a samples, the peaks at 3420 and 1626 cm^{-1} disappeared completely, and two new sharp bands appeared at 575 and 485 cm^{-1} due to the formation of α-Fe_2O_3. The FTIR results indicated the formation of α-Fe_2O_3 after heating the samples at 300 °C and 500 °C for 24 hr [37].

3.1.2. Thermal analysis

Figure 4 shows TGA diagrams of the as-prepared samples containing PEO polymers with different molecular weights (S1a, S1b, and S1c). All curves exhibited one main weight loss region from

120 °C–600 °C. No change in weight loss was observed until 150 °C, when a slight temperature loss of approximately 0.5–1.7% was observed. This could be attributed to the desorption of coordinately bonded water molecules or physically bonded hydroxide groups [38]. Upon further heating, the weight loss increased and reached approximately 8%, which may be attributed to the decomposition and burning of the PEO molecules. A weight loss of approximately 10.58% was observed at a temperature of 280 °C–330 °C, which could be due to the complete decomposition and removal of the PEO molecules and the thermal dehydration of any inorganic particles. No other weight loss was observed after 500 °C [39]. From these results, it was clear that all polymer molecules were removed from the sample powder after the heat-treatment process at ~ 300 °C.

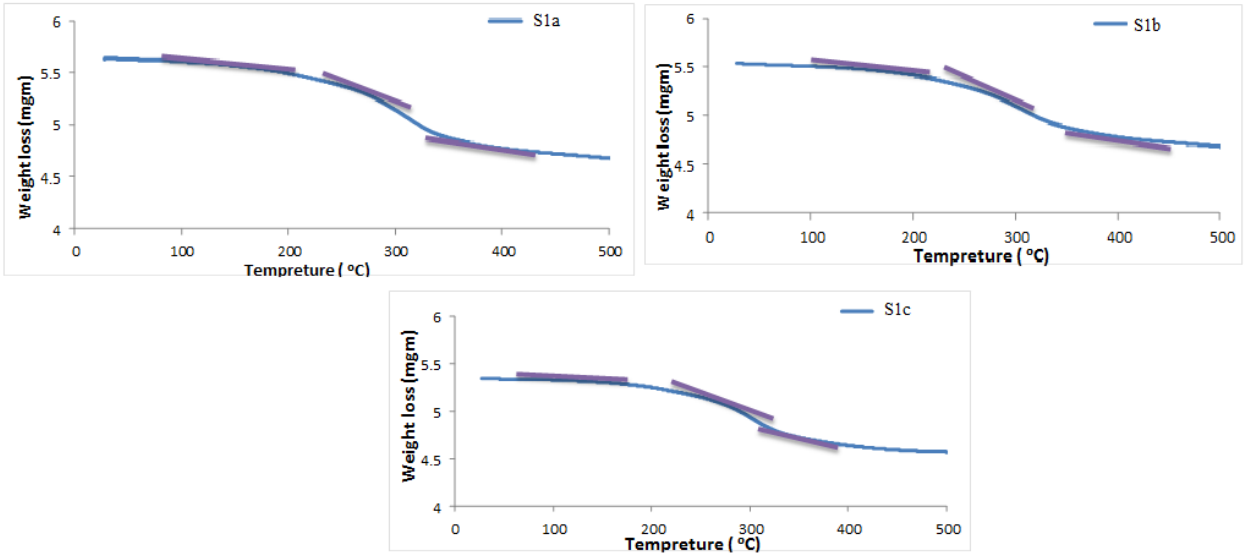

Figure 4. TGA diagrams of the as-prepared samples in the presence of PEO polymer with different molecular weights: S1a, S1b, and S1c.

3.1.3. Morphological structure

Figure 5 presents the morphological structures of the as-deposited samples as well as the heat-treated samples. For sample S1a, the film had very small spindle-like nanoparticles of β-FeOOH with sizes in the range 55–65 nm with large particles of PEO. Irregular spherical particles of α-Fe_2O_3 with diameters of 100–150 nm were observed in samples S2a and S3a. The porosity of these samples increased due to the removal of the PEO particles by burning. [40,41].

Large PEO particles act as stabilizers for iron oxide nanoparticle chemistries and/or architectures and provide the desired surface properties of a given material.

Many recurring units are present in the PEO backbone, each of which can exhibit different functions of iron oxide nanoparticles. Such polymers have great potential for stabilizing iron oxide nanoparticles due to their multivalence.

The use of PEO is associated not only with stability but also with providing suitable synthetic conditions and the ability to resize and shape the nanoparticles [42].

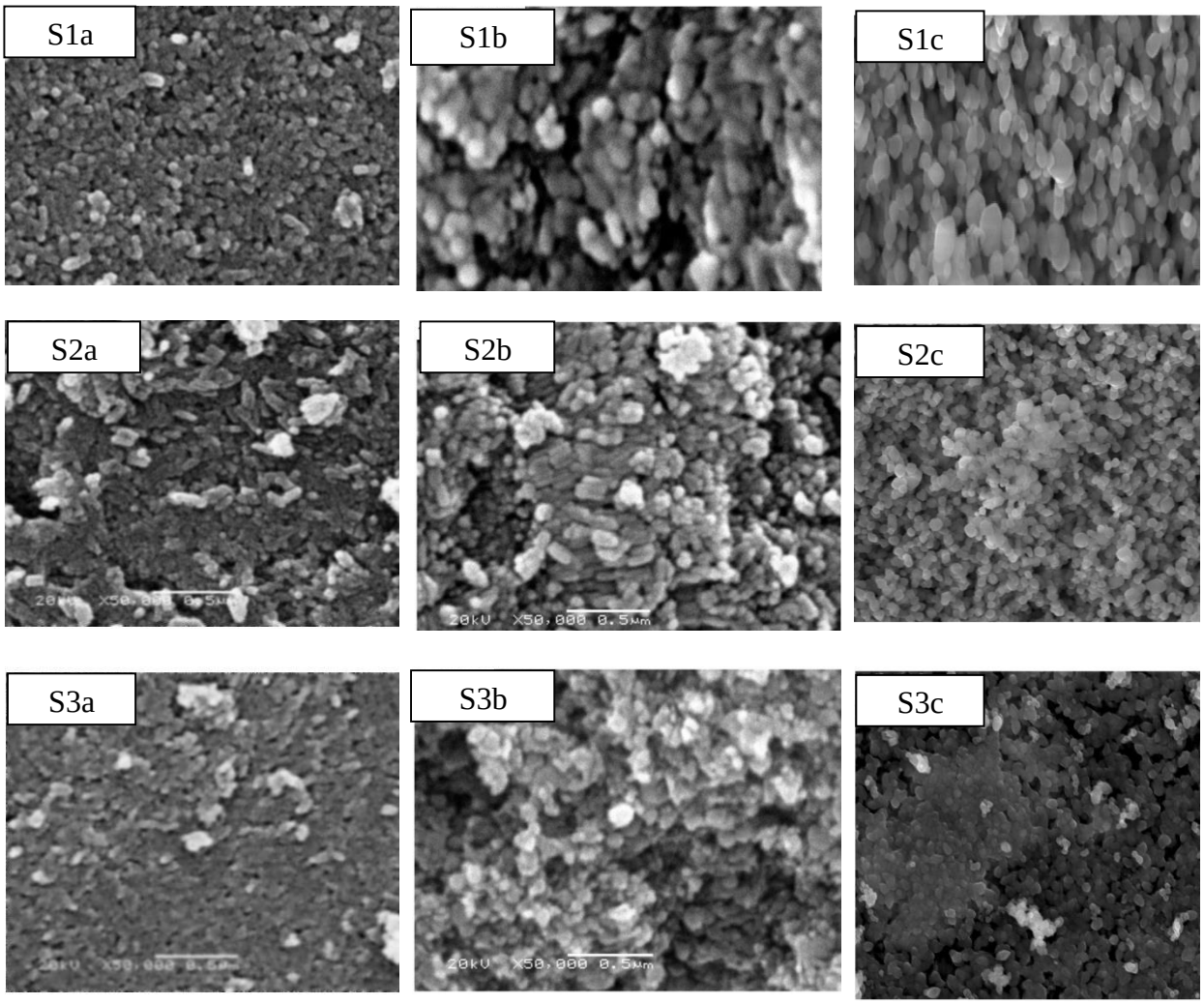

Figure 5. SEM images of the as-prepared and heat-treated samples (using PEO with different molecular weights) (all images; 50000X, 20 kV).

Sample S1b shows spindle nanoparticles of β-FeOOH with large PEO particles, while Sample S2b shows the presence of 1D bundle-like nanorods with widths of 14.29 nm and lengths of 25 – 53 nm. The β-FeOOH particles transformed into α-Fe_2O_3, and the PEO particles were removed by heat treatment. The bundle-like architecture became well maintained. For the S3b sample, large spindle-like particles were observed due to the complete transformation of all β-FeOOH into α-Fe_2O_3 during heat treatment. Sample S1c shows small bundle-like nanorods, while samples S2c and S3c show a mixture of nanoparticles and nanorods. The formation of bundle-like nanorods during the hydrothermal synthesis of α-Fe_2O_3 proceeds in successive steps, including nucleation, surface regulation, growth, and oriented attachment. Initially, crystal nucleates emerged from a pre-existing solution, and growth occurred simultaneously. PEO C-O groups easily attach to the surface of the crystal surface and reduce the crystal growth rate at a given crystallographic orientation [43,44]. Under the capping effect of PEO, crystals preferentially grow along the chain of PEO, and finally, rod-like crystals will form with direct-directed attachments. As a result of the van der Waals attraction effect [45], the rod-like structure tends to coalesce and form bundle-like α-Fe_2O_3 nanostructures, which form after β-FeOOH heat treatment without deformation in the structure and become rough [40].

Figure 6 shows the TEM images and the selected area electron diffraction (SAED) of sample S2b. The choice of this sample was attributed to the complete transformation of β-FeOOH to the bundle-like α-Fe_2O_3 nanostructures that were confirmed by SEM.

The figure shows that the α-Fe_2O_3 particles are well dispersed and have a bundle-like nanorod structure with a width ranging from 11.04 nm to 16.17 nm and a length range of 29–60 nm. The SAED pattern of the S2b sample showed clear diffraction spots, indicating the high degree of crystallinity of the hematite nanoparticles [46,47]. The formation of a well-dispersed, bundle-like-nanorod iron oxide structure was attributed to the growth of large crystals and presence of less strain among the particles during synthesis.

According to previous data, samples S1b, S2b, and S3b are preferred for use as ARC materials due to their structure and morphology.

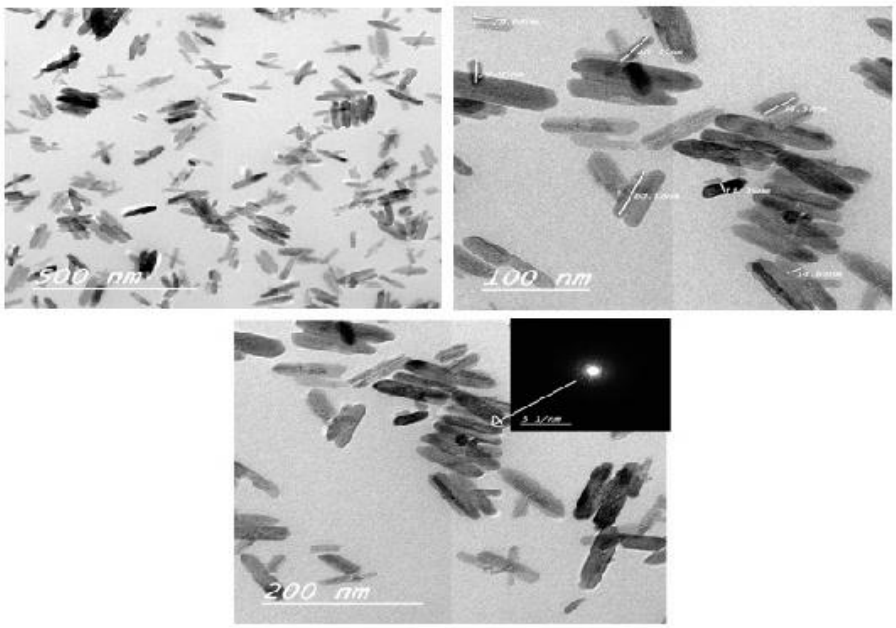

Figure 6. HRTEM images and SAED pattern of the S2b sample.

3.1.4. Optical analysis

The optical transmission of all samples is recorded as a function of the wavelength, and the maximum transmissions are shown in Table 1 and Figure 7. Sample S1b has an optical transmission of 91% due to the presence of polymer molecules and the formation of β-FeOOH during hydrothermal synthesis. The presence of polymer molecules leads to the reflection of the incident light, reducing the optical transmittance.

For sample S2b, the polymer molecules were removed by burning, and β-FeOOH was converted into α-Fe_2O_3 with irregular spherical particles. This leads to an increase in transmittance to the maximum value of 94.4% due to the formation of well-defined bundle-like nanorods. This reduced the reflectance

of the incident light and facilitated the passage of the light through the pores formed during heat treatment.

For S3b, the change in surface morphology due to the increase in particle size of α-Fe_2O_3 caused reflection of some of the incident light, reducing the optical transmittance.

It is clear that the increase in temperature in the heat treatment process from 300 to 500 °C reduces the optical transmittance from 94.4% to 91%. This can be caused by an increase in particle size and therefore an increase in the reflectance of the samples [48].

Table 1. Optical transmittance of the as-prepared and heat-treated samples.

Samples		T(%)
As-prepared	S1a	90.65
	S1b	90.65
	S1c	91.4
Heat treatment at 300 °C for 24 hr	S2a	94.0
	S2b	94.4
	S2c	93.7
Heat treatment at 500 °C for 24 hr	S3a	91.4
	S3b	90.7
	S3c	91.2

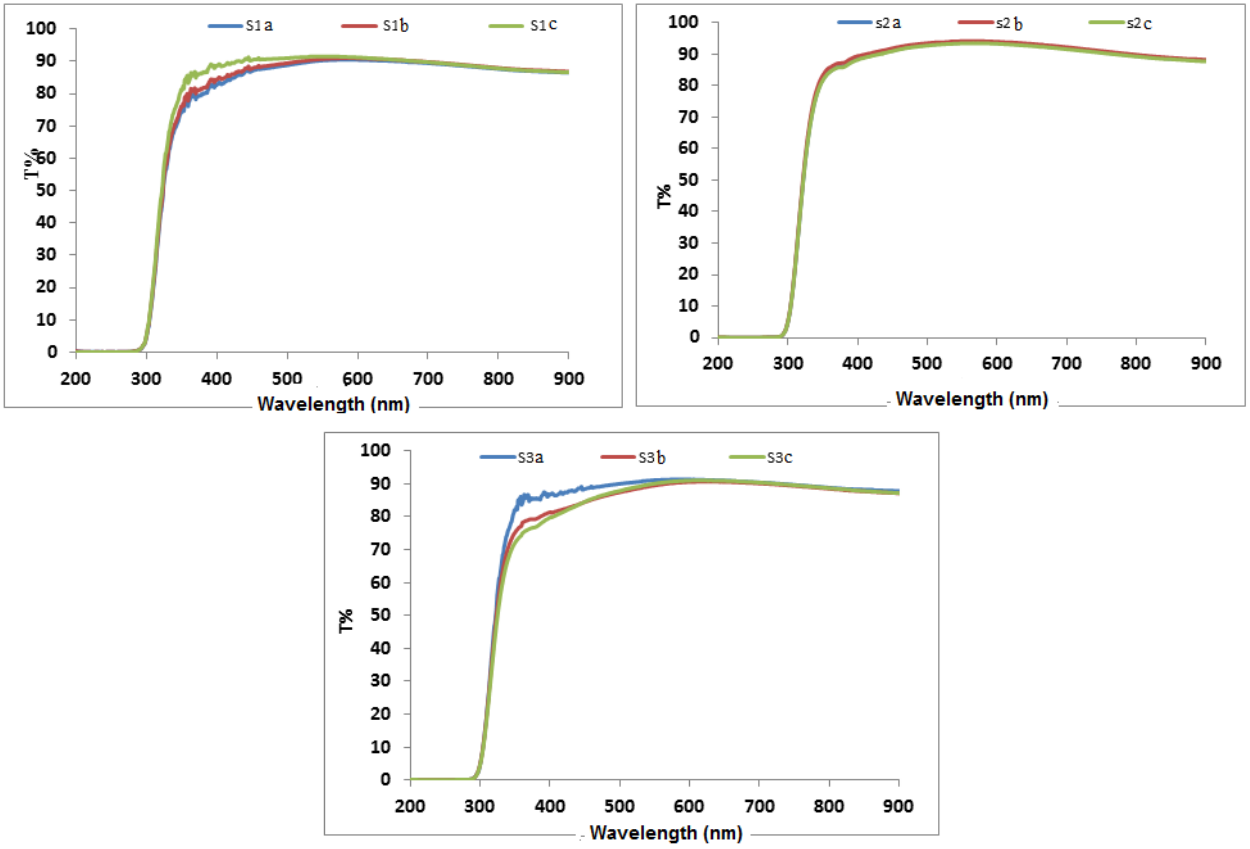

Figure 7. Optical transmittance spectra of samples.

3.2. Performance of DSSC cells

Figure 8 and Table 2 show the current density–voltage (J–V) characteristic curves of the DSSCs without and with an antireflection layer of α-Fe_2O_3 (heat treatment at 300 °C for 24 hr and after the addition of PEO (100k MW) deposited on the glass side of ITO glass substrates under an illumination light intensity of 100 mW/cm^2). The efficiency η of the cell can be obtained by Equation (5).

For normally incident illumination light, the J_{SC} of the device improves by ~24%, which leads to an efficiency rise of ~25%.

The results confirmed that the incorporation of α-Fe_2O_3 ARC layers in DSSCs significantly increased the short-circuit current density (J_{SC}) and the efficiency (η). Improvement in J_{SC} can be explained by using nonlinear relations between the number of carriers created as a result of increased photon absorption [49–51]. Table 3. Shows a comparison between the effects of using different ARC materials on the performance efficiency of DSSCs.

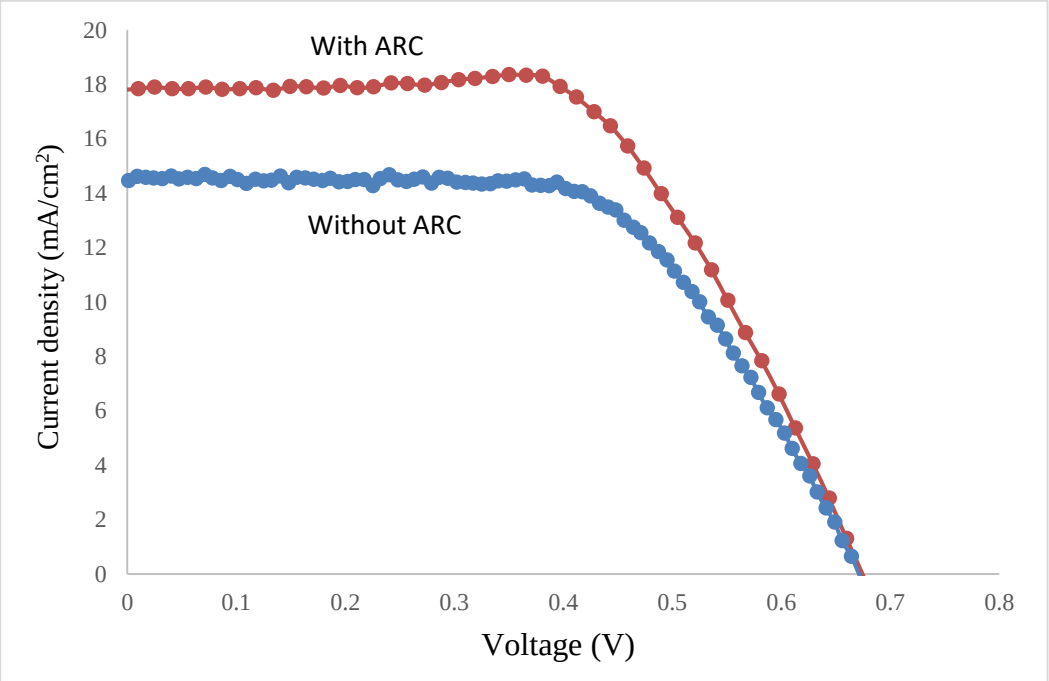

Figure 8. J–V curves of the DSSCs without and with the α-Fe_2O_3 layer used as an ARC**.**

Table 2. Current density–voltage (J–V) characteristic curves of the DSSCs without and with an antireflection layer of α-Fe_2O_3.

Device	V_{oc} (mV)	J_{sc} (mA/cm^2)	FF	η (%)
α-Fe_2O_3 ARC	675	17.81	0.607	7.3
DSSC	671.5	14.45	0.61	6

Table 3. Effects of using different ARC materials on the performance efficiency of DSSCs.

ARC materials	Efficiency improvement (%)
Diamond-like carbon (DLC) thin films [51]	4.92% to 5.35%
MgF2 [9]	7.37 to 7.89
polydimethylsiloxane (PDMS) polymer [52]	7.15% to 7.56%
ZnO [53]	1.19% to 1.54%
SiO2 [54]	4.76% to 6.03%
ZnO-SiO2 [55]	4.67% to 5.79%
Silica nanoparticles [56]	6.03 to 6.64%

4. CONCLUSIONS

- The α-Fe_2O_3 nanopowder was prepared by the hydrothermal (HT) method from acidified $FeCl_3$ solution. The effects of heat treatment and polymer addition with different molecular weights on the properties of the produced powder sample were studied.
- The XRD patterns indicated that the structure of α-Fe_2O_3 was hexagonal and that its crystallinity increased after heat treatment at 300 °C for 24 hr.
- Bundle-like α-Fe_2O_3 nanorods with widths ranging from 11.04 nm to 16.17 nm and lengths in the range of 29–60 nm formed by the addition of PEO during the hydrolysis process.
- The optimum parameters used to prepare the α-Fe_2O_3 layer with a high optical transmittance of 94.4% were as follows: deposition of one layer at immersion intervals of 5 min with 300 °C heat treatment using 2.5 mg of α-Fe_2O_3 as a precursor with the addition of PEO (100k MW)
- The short circuit current of the DSSC was improved from 14.45 to 17.81 by using the Fe_2O_3 layer as an antireflection coating.

AUTHOR CONTRIBUTIONS

Conceptualization; Marwa Fathy, Ahmed I Omran. Investigation; Said S. El Egamy, Marwa Fathy, and Ahmed I Omran. Methodology; Marwa Fathy, Ahmed I Omran. Supervision, Said S. El Egamy, Marwa Fathy. Visualization, Said S. El Egamy, Marwa Fathy. Writing—review & editing, Said S. El Egamy, Marwa Fathy, and Ahmed I Omran.

FUNDING

This research received no external funding.

CONFLICTS OF INTEREST

The authors declare that they have no known competing financial interests or personal relationships that could have appeared to influence the work reported in this paper and no conflicts of interest.

ACKNOWLEDGEMENT

The authors acknowledged Professor Waheed A. Badway (mercy upon him), Chemistry Department, Faculty of Science, Cairo University. The authors wish to express their thanks to the Chemistry Department, Faculty of Science, Cairo University, and the Department of Electronic Materials, Institute of Advanced Technology and New Materials, City of Scientific Research and Technological Applications, for their contributions to the accomplishment of this research.

References

1. W. Joo, Y. Kim, S. Jang, and J. Kim, *Thin Solid Films,* 519 (2011) 3804.
2. W.L. Min, B. Jiang and P. Jiang, *Adv. Mater.,* 20 (2008) 3914.
3. Y. Li, F. Li, J. Zhang, C. Wang, S. Zhu, H. Yu, Z. Wang, and B. Yang, *Appl. Phys. Lett.,* 96(2010) 153305.
4. Q. Mu, Y. Li, H. Wang and Q. Zhang*, J. Colloid Interface Sci.,* 365 (2012) 308.
5. Y. Lu, X. Zhang, J. Huang, J. Li, T. Wei, P. Lan, Y. Yang, H. Xu and W. Song, *Optik-International J. Light, and Electron Optics,* 124 (2013) 3392.
6. M.-L. Kuo, D.J. Poxson, Y.S. Kim, F.W. Mont, J. K. Kim, E.F. Schubert and S-Y. Lin, *Opt. Lett.,* 33 (2008) 2527.
7. K. Sharma, V. Sharma, and S.S. Sharma, *Nanoscale Res. Lett.,* 13 (2018) 381.
8. N. Shanmugam, R. Pugazhendhi, R.M. Elavarasan , P. Kasiviswanathan and N. Das, *Energies,* 13 (2020) 2631.
9. J.E. Nam, H.J. Jo, D-H Son, D-H Kim and J-K Kang, *Applied Mechanics and Materials,* 705 (2015) 320.
10. Q. Zhang, J. Wang, G. Wu, J. Shen and S. Buddhudu, *Mater. Chem. Phys.,* 72 (2001) 56.
11. P. Nostell, A. Roos and B. Karlsson, *Thin Solid Films,* 351 (1999) 170.
12. A. Gombert , W. Glaubitt , K. Rose , J. Dreibholz , C. Zanke , B. Blasi , A. Heinzel , W. Horbert , D. Sporn and W. Doll, *Sol. Energy,* 62 (1998) 177.
13. D.R. Uhlmann, T. Suratwala, K. Davidson, J.M. Boulton, and G. Teowee, *J. Non-Cryst. Solids,* 218 (1997) 113.
14. J.A Hiller, J.D. Mendelsohn and M.F. Rubner, *Nat. Mater.,* 1(2002) 59.
15. J.H. Rouse and G.S. Ferguson, *J. Am. Chem. Soc.,* 125(2003) 15529.
16. J.-W. Kim, R.J. Larsen, and D.A. Weitz, *J. Am. Chem. Soc,* 128 (2006) 14374.
17. H.L. Chen, S.Y. Chuang, C.H. Lin, and Y.H. Lin, *Opt. Express,* 15 (2007) 14793.
18. A.S. Dimitrov, T. Miwa and K. Nagayama, *Langmuir,* 15 (1999) 5257.
19. A. Qurashi, Z. Zhong and M.W. Alam, *Solid State Sci.,* 12(2010)1516.
20. J. Chen, L.N. Xu, W. Li, and X. Gou, *Adv. Mater.,* 17 (2005) 582.
21. B. Sun , J. Horvat, H.S. Kim, W.-S. Kim, J. Ahn and G. Wang, *J. Phys. Chem. C,* 114 (2010) 18753.
22. T. Cheng, Z. Fang, Q. Hu, K. Han, X. Yang, and Y. Zhang, *Catal. Commun.,* 8 (2007) 1167.
23. F. Bondioli, A.M. Ferrari, C. Leonelli and T. Manfredini, *Mater. Res. Bull.,* 33 (1998) 723.
24. S. Mitra, S. Das, K. Mandal, and S. Chaudhuri, *Nanotechnology,* 18 (2007) 275608.
25. M. Fathy, A. I. Omran, and W. A. Badway, *Int. J. Sci.,* 3 (2016) 127.
26. W. Dong and C. Zhu, *J. Mater. Chem.,* 12 (2002) 1676.
27. A.B. Kashyout, M. Fathy and M.B. Soliman, *Int. J. Photoenergy,* (2011) 139374
28. A.B. Kashyout, M. Soliman and M. Fathy, *Renewable Energy,* 35 (2010) 2914.
29. T. Almeida, “Hydrothermal synthesis and characterization of α-Fe2O3 nano-rods", Ph.D. thesis, University of Nottingham, 2010.
30. X.Q. Liu, S.W. Tao, and Y.S. Shen, *Sens. Actuators, B,* 40(1997) 161.
31. C.M. Flynn, *Chem. Rev.,* 84 (1984) 31.
32. Q.Y. Zhang, J. Wang, G. Wu, J. Shen, and S. Buddhudu, *Mater. Chem. Phys.* 72 (2001)56.
33. S. Sultana, M.S. Khan and M. Humayun, *Chem.,* 36 (2012) 709.
34. D.E. Hegazy and G.A Mahmoud, *Arb J. Nucl. Sci. Appls.,* 47 (2014) 14
35. V. M. Mohan, V. Raja, A. K. Sharma, and V.V.R. Narasimha Rao, *Ionics* 12 (2006) 219.
36. B. Richards, *Prog. Photovoltaics Res. Appl.,* 12 (2004) 253.
37. V. Uvarov and I. Popov, *Mater. Charact.,* 58 (2007) 883.
38. N.K. Singh, M.L. Verma, and M. Minakshi, *Bull. Mater. Sci.,* 38 (2015) 1577.
39. T. Caykara, S. Demirci, M. Eroglu and O. Güven, *Polymers,* 46 (2005) 10750.
40. P. Sun, L. You, D. Wang, Y. Sun, J. Ma and G. Lu, *Sens. Actuators, B,* 156 (2011) 368.

41. W. Joo, M.S. Park and J.K. Kim, *Langmuir,* 22 (2006) 7960.
42. S. Razzaque, S.Z. Hussain, I. Hussain, B. Tan, *Polymers,* 8 *(*2016) 156.
43. H-W. Chen, C-H. Jiang, H-D. Wu, F-C. Chang, *J Appl. Polym. Sci.,* 91 (2004) 1207.
44. T. Almeida, "Hydrothermal synthesis and characterization of α-Fe_2O_3 nano-rods", A thesis submitted to the University of Nottingham (2010).
45. A.S. Dimitrov, T. Miwa and K. Nagayama, *Langmuir,* 15(1999) 5257.
46. J. Mohapatra, A. Mitra, H. Tyagi, D. Bahadur and M. Aslam, *Nanoscale,* 7 (2015) 9174.
47. M.M. Rahman, S.B. Khan, A. Jamal, M. Faisal, and A.M. Aisiri, "Iron Oxide Nanoparticles, Nanomaterials",DOI: 10.5772/27698. https://www.intechopen.com/books/nanomaterials/iron-oxide-nanoparticles
48. R.T. Rasheed, S.D. Al-Algawi, H.H. Kareem and H.S. Mansoor, *J. Chem. Sci.,* 9 (2018).
49. R. Sharma, A. Gupta, and A. Virdi, *J. Nano & Electron. Phys.,* 9 (2017) 02001-1.
50. J.E. Nam, H.J. Jo, D.H. Son, D-H. Kim and J-K. Kang, *Appl. Mech. & Mater.,* 705 (2015) 320.
51. J-S Song, Y.S Park, and N-H. Kim, *Appl.Sci.,* 11 (2021) 358.
52. J.H. Lim, J.W. Leem and J.S. Yu, *RSC Adv.*, 5 (2015) 61284.
53. E. Chanta, C. Bhoomanee, A. Gardchareon, D. Wongratanaphisan, S. Phadungdhitidhada and S. Choopun, *J. Nanosci. Nanotechnol*., 15 (2015) 7136.
54. C.-N. Chen, M.-J. Wu, C.-F. Hsu and J.-J. Huang, *Surf. Coat. Technol.,* 320 (2017) 28.
55. D. Li, F. Huang and S. Ding, *Appl. Surf. Sci.,* 257 (2011) 9752.
56. W. Li, X. Tan,; J. Zhu, P. Xiang, T. Xiao, L.Tian, A. Yang, M. Wang and X. Chen, *Mater. Today Energy*, 12 (2019) 348.